Finite-difference P wave travel time seismic tomography of the crust and uppermost mantle in the Italian region

L. Gualtieri, P. Serretti, A. Morelli

Finite-difference *P* wave travel time seismic tomography of the crust and uppermost mantle in the Italian region

L. Gualtieri

Institut de Physique du Globe de Paris, 1 Rue Jussieu, FR-75005 Paris CEDEX 05, France

Dipartimento di Fisica e Astronomia, Settore di Geofisica, Università di Bologna, Bologna, Italy (gualtieri@ipgp.fr)

P. Serretti and A. Morelli

Istituto Nazionale di Geofisica e Vulcanologia, Bologna, Italy

[1] We present a 3-D *P* wave velocity model of the crust and shallowest mantle under the Italian region, that includes a revised Moho depth map, obtained by regional seismic travel time tomography. We invert 191,850 P_n and P_g wave arrival times from 6850 earthquakes that occurred within the region from 1988 to 2007, recorded by 264 permanent seismic stations. We adopt a high-resolution linear B-spline model representation, with 0.1° horizontal and 2 km vertical grid spacing, and an accurate finite-difference forward calculation scheme. Our nonlinear iterative inversion process uses the recent European reference 3-D crustal model EPcrust as a priori information. Our resulting model shows two arcs of relatively low velocity in the crust running along both the Alps and the Apennines, underlying the collision belts between plates. Beneath the Western Alps we detect the presence of the Ivrea body, denoted by a strong high *P* wave velocity anomaly. We also map the Moho discontinuity resulting from the inversion, imaged as the relatively sharp transition between crust and mantle, where *P* wave velocity steps up to values larger than 8 km/s. This simple condition yields an image quite in agreement with previous studies that use explicit representations for the discontinuity. We find a complex lithospheric structure characterized by shallower Moho close by the Tyrrhenian Sea, intermediate depth along the Adriatic coast, and deepest Moho under the two mountain belts.

1. Introduction

[2] The Italian peninsula plays a fundamental role in the geodynamic evolution of the Mediterranean region. The two main Italian mountain chains—the Alps and the Apennines, Figure 1—are due to complex processes generated by large-scale convergence between the African and Eurasian plates,
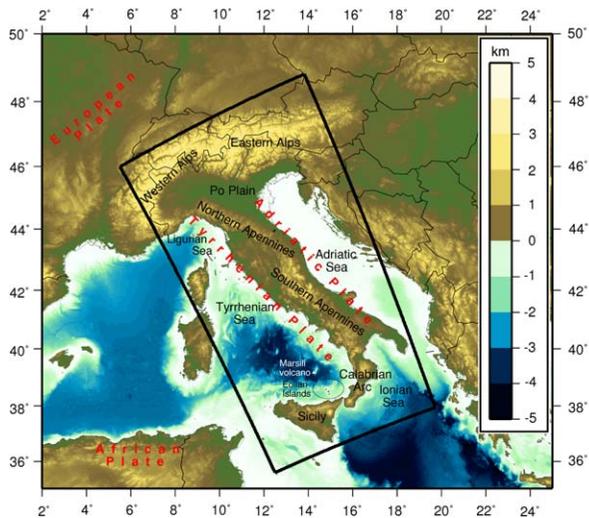
Figure 1. Map of the Italian peninsula in the central Mediterranean topographic context. In black we mark the toponyms and in red the tectonic plates. Only the region inside the black rectangle is taken into account during the computation and it denotes the studied region.

since about 65 My ago [e.g., *Malinverno and Ryan*, 1986; *Faccenna et al.*, 2004]. These processes have pushed lithospheric material beneath the Alps, Apennines, and the Calabrian Arc. Substantial agreement exists over the formation of the Alps as a consequence of the closure and ensuing subduction of the Alpine Tethyan domain [e.g., *Schmid et al.*, 2005; *Handy et al.*, 2010]. Several competing models have been proposed to explain the formation of the Apennines that have either been related to westward directed subduction since the Cretaceous, or thought to have developed along the retrobelt of the south-westward prolongation of the Alps [*Carminati and Doglioni*, 2012]. *Benoit et al.* [2011] suggest instead a delamination scenario for the northern part of the Apennines and the presence of a slab foundering at its northern terminus.

[3] In recent years, several seismological studies have revealed with increasing detail the seismic velocity structure of the mantle inverting both regional and teleseismic data in this crucial part of the Mediterranean. Among the most striking features, lithospheric slabs subducting into the upper mantle have been mapped as high v_P and v_S bodies under the Apennines [e.g., *Amato et al.*, 1993; *Lucente et al.*, 1999; *Cimini and De Gori*, 2001; *Piromallo and Morelli*, 2003; *Montuori et al.*, 2007] and the Alps [e.g., *Piromallo and Morelli*, 2003; *Lippitsch et al.*, 2003; *Kissling et al.*, 2006; *Wagner et al.*, 2012]. These studies reveal the

presence of a lithospheric slab below 100 km, but fail to resolve it unambiguously in its shallow extent. Regional tomographic studies, such as *Mele et al.* [1998], *Di Stefano et al.* [1999], *Piromallo and Morelli* [2003], and *Di Stefano et al.* [2009], have also provided information about the lithosphere-asthenosphere system, and have shown the presence of both fast and slow anomalies beneath the Italian region.

[4] The structure of the crust is not often retrieved in these studies, and models of its constitution are frequently used only as a fixed constraint. At this scale, comprehensive information about thickness, density, and seismic velocities in the crust is still rather poor, or missing spatial continuity. Studies about crustal thickness, or Moho structure, have been conducted using receiver functions [e.g., *Piana Agostinetti et al.*, 2002; *Mele et al.*, 2003; *Piana Agostinetti and Amato*, 2009; *Di Stefano et al.*, 2011], measuring crustal thickness beneath several seismic stations. *Piana Agostinetti et al.* [2008] and *Bianchi et al.* [2010] have found a dipping interface that marks the top of the Apennines slab at 40–80 km. Such determinations, however, represent Moho depth at single points, and do not provide a laterally continuous model unless through interpolation across wide geographical gaps [*Piana Agostinetti and Amato*, 2009].

[5] The aim of this paper is improve the knowledge of the crustal structure of Italy through seismic travel time tomography, for which we focus our attention to the shallowest 50 km. In our study we use travel times of *P* waves from earthquakes located inside the model region, retrieved from the EHB seismic catalog [*International Seismological Centre* (*ISC*), 2009]. As we follow a nonlinear iterative inversion process, with full 3-D finite-difference forward travel time calculation, a reliable initial model is needed. For this reason, we opt to use the recent 3-D European reference model EPcrust [*Molinari and Morelli*, 2011] as our a priori. Our model consists of an image of *P* wave velocity interpolated on a 3-D grid of nodes, where we can identify the surface of the Moho as the locus of sharp increase of seismic velocity. In the following, we describe our data and methods, show results of recovery tests and inversion of real data, and finally provide a discussion of results.

2. Data and Method

[6] We consider *P* wave travel times retrieved from the EHB Bulletin of the International
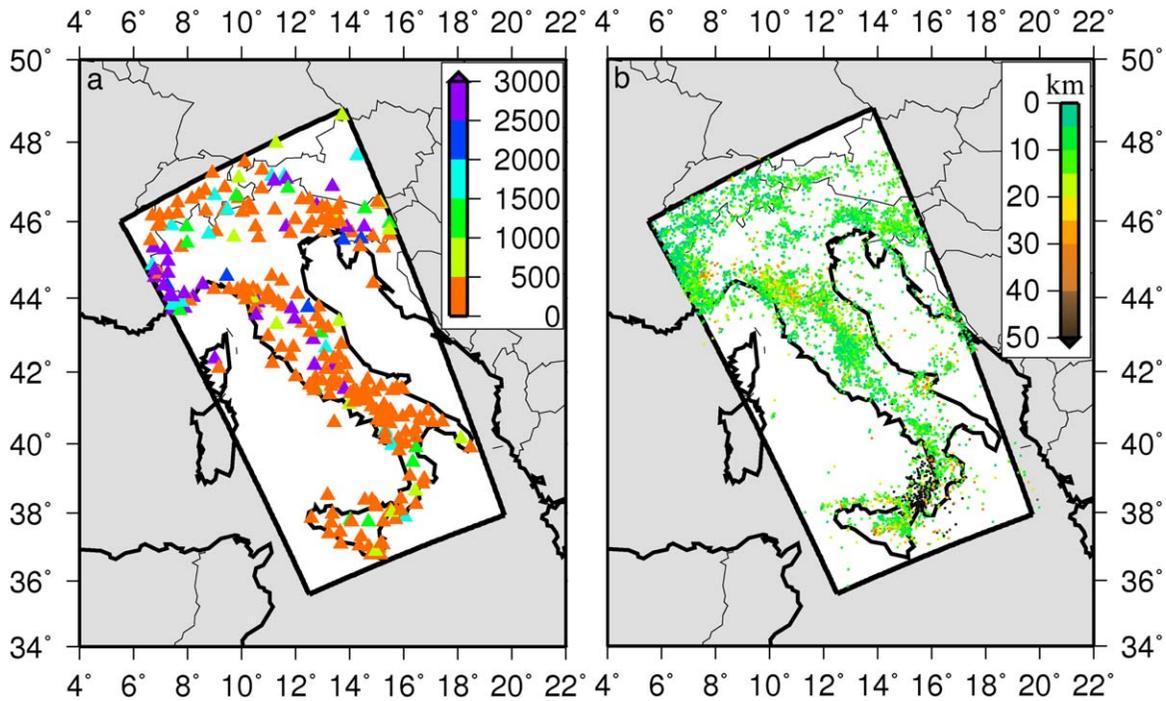
Figure 2. (a) Seismic stations. The color scale shows the number of recorded events. (b) Earthquakes epicentres. The color scale shows the hypocentral depth. Only the region inside the black rectangle is taken into account during the computation and it denotes the studied region.

Seismological Centre [*ISC*, 2009] for the time period between 1988 and 2007. The well-known EHB Bulletin is a ISC-based earthquake catalog reprocessed and updated by *Engdahl et al.* [1998]. The processing of *Engdahl et al.* [1998] composed of an iterative relocation with dynamic phase identification in a 1-D Earth reference model [ak135, *Kennett et al.*, 1995]. We select both earthquakes and seismographic stations falling inside our study area, covering the whole Italian peninsula, stretching 1300 km in latitude and 700 km in longitude, and extending from the Alps to the Calabrian Arc and Sicily (Figure 1). We end up with 264 stations (see Figure 2a). The Italian region is well covered by seismic stations, although we may note a gap in the distribution in the Po Plain. We select only earthquakes having a resulting station coverage with a secondary azimuthal gap smaller than 180°. Finally, we reject stations with fewer than five records. The total number of events chosen—and then used during the inversion step—is 6850, with 191,850 total seismic rays, resulting in 28 stations recording the same event on average. According with Figure 2a, about 69% of the stations record less than 500 events. We consider the first arrivals, corresponding both to P_n and P_g phases. The data set provides good coverage down to about 50 km depth.

[7] Figure 3 shows the path distribution as a function of epicentral distance (top) and path density as a function of depth (bottom), as calculated in our a priori model, following the technique that we describe further on. Deeper than 50 km, the ray coverage becomes insufficient to provide good resolution. The picture shows peaks of seismic ray density just below the average depth of the main discontinuities of the velocity field. In particular, we observe an increase of the average seismic ray density at the depth of 4 km, where a discontinuity between sedimentary layer and crystalline upper crust is generally present, and at the depth of 14–16 km, corresponding to upper/lower crust transition. The main peak at about 36–38 km depth is where P_n waves concentrate. The Moho region is therefore very well sampled and we may expect to be able to map structure in its vicinity with best accuracy.

[8] We calculate first-arrival travel times using a finite-difference method based on numerical solution on a 3-D grid of the eikonal equation and propagation of the first-arrival wavefront [*Vidale*, 1988, 1990; *Podvin and Lecompte*, 1991]. We specifically use the algorithm proposed by *Podvin and Lecompte* [1991] that is able to account for the existence of different wave propagation
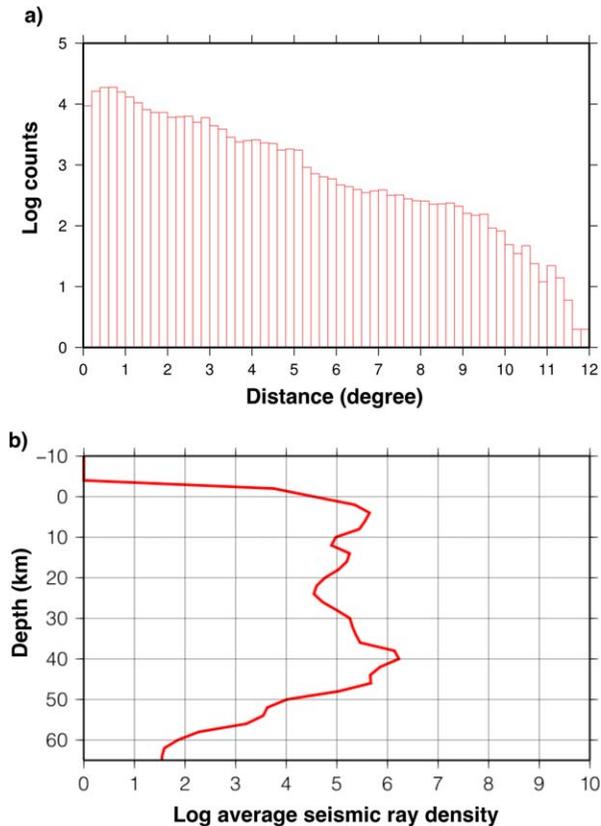
Figure 3. (a) Ray frequency as a function of epicentral distance. (b) Corresponding distribution of average seismic ray density as a function of depth. Density is calculated as an average of the total ray length within model blocks at a given depth. Coverage is best down to about 50 km and it has a peak at 30–40 km depth, corresponding to the depth range just beneath the Moho discontinuity, due to wide diffusion of *Pn* phases.

modes, in its updated version given by *Tryggvason and Bergman* [2006] to guarantee reciprocity of travel time for stations located close to an anomaly region. Upon retrieval of the whole travel time field, the raypath may be back-tracked following the travel time gradient from station to hypocenter to find the seismic raypath. By making use of the reciprocity property of ray-theoretical travel times, for each station we calculate the travel time field originating at each station. The raypath, for each station-event pair, is then calculated following the gradient of the wavefront. Following the approach detailed by *Serretti and Morelli* [2011], we compute the gradient to wave fronts by finite differences [e.g., *Lapidus and Pinder*, 1982].

[9] This method requires discretization of the velocity field in a 3-D Cartesian grid with cubic cells with constant velocity (or slowness). Obviously, the precision of travel times and raypaths

depends on the grid step size. Following the numerical tests shown by *Serretti and Morelli* [2011], and favoring precision with respect to computational cost, we choose a uniform step size for our grid of 1 km in each direction. The limited regional range of the model makes the calculation quite manageable. This computational grid is used for the finite-difference discretization, needed to solve the forward problem, and is independent from the model description—that can be coarser for economy in the inversion stage—as illustrated further on. The slowness to be assigned to each computational element is defined by a linear B-spline interpolation within the model grid. For convenience, we rotate the geographical reference frame to a new system, with a new North aligned along the main axis of the box. The computational grid size is thus 1300 km × 700 km × 300 km along rotated latitude, longitude, and depth (see Figure 2). We take into account Earth curvature by applying the Earth flattening approximation, and we use an equidistant azimuthal projection to map the Cartesian grid to the sphere [*Serretti and Morelli*, 2011]. Advantages of the use of the numerical solution of the eikonal equation, over approximate ray tracing techniques, are particularly evident in the presence of strong velocity gradients—such as in crust and uppermost mantle environments—where it handles the nonlinear dependence of the travel time on the velocity field in full.

[10] The seismic velocity model is represented by a grid of nodes, where actual *P* wave speed is specified, and a linear B-spline interpolation is used to give velocity at any point within each cell. The model grid step is 0.1° in both latitude and longitude, and 2 km in the vertical direction. The model thus consists of 231 × 151 × 301 nodes, for a total of 10,499,181 model parameters. We chose this parameterization in order to represent small heterogeneities as well as sharp velocity gradients—such as the transition from crust to mantle. Note that this parametric continuous representation of the 3-D velocity field (the tomographic model) needs to be discretized by the finite-difference computational grid, as described above. The thin vertical spacing of the model parameterization grid is necessary to work with a structural model without an explicit discontinuity, and consisting of a 3-D continuous wave speed field. We do need a fine vertical spacing both to be able to locate the Moho with sufficient precision, and to keep the discontinuity—actually, a strong gradient in our model (see section 4.1)—sharp enough. Using an adequate inversion approach, as shown
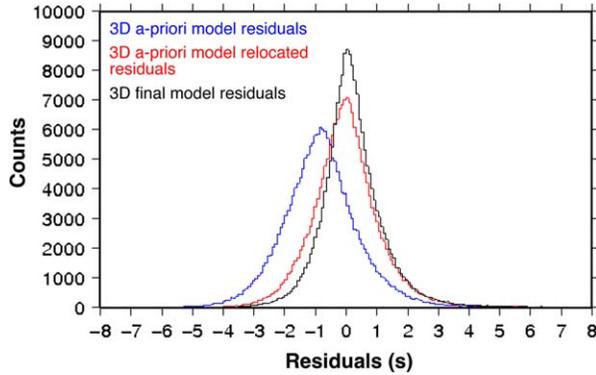
Figure 4. Histograms of travel time residuals at different stages of the inversion. Blue: initial residuals; red: residuals after the preliminary relocation; black: final residuals after model inversion. The mean value drops from -0.812 s to 3.58×10^{-3} s after the origin time relocation and it remains stable in the final model. The RMS reduces from 1.63 s (blue histogram) to 1.22 s (black histogram). After the origin time relocation the RMS is 1.34 s (red histogram).

further on, the number of parameters used to represent the model does not pose critical issues [for a review, see e.g., *Tarantola*, 2005].

[11] We use the recent European plate 3-D reference crustal model EPcrust [*Molinari and Morelli*, 2011] as our a priori information. EPcrust integrates local information from a variety of previous high-resolution studies and provides seismic speeds (*P* and S) and density in variable-thickness sedimentary and crystalline layers, with a sharp Moho. We use seismic wave speeds in the underlying mantle from *sp6* [*Morelli and Dziewonski*, 1993].

[12] To locate the sources and perform calculations, we keep into account the real elevation of seismic stations and apply corrections for ellipticity of the Earth. We perform a preliminary relocation of all seismic events in this model. For each source, we calculate travel times to all seismographic stations using the method illustrated above, and then correct the origin time to obtain a zero average of all the time residuals. This origin time-relocation step is needed to discard a possible bias between the global 1-D Earth model in which the data set has been located by *Engdahl et al.* [1998], and our regional 3-D crustal model. Figure 4 shows a frequency histogram of seismic travel time residuals before (blue curve) and after (red curve) this origin time relocation. The mean value drops from -0.812 to 3.58×10^{-3} s, whereas the RMS from 1.63 s reduces to 1.34 s. We observe that the seismic travel time residuals computed

before the origin time relocation have a systematic negative shift meaning that, for this particular region, as average, seismic rays have a tendency to travel slower in our a priori model with respect to the 1-D model used for relocating events in the EHB Bulletin.

[13] Our aim is then to find a model, **m**, able to predict observed travel times, $\mathbf{d}_{obs}$, within uncertainties given by a data covariance matrix, $\mathbf{C}_D$, given that we are able to compute travel times in a candidate model $\mathbf{m}_n$ as: $\mathbf{d}_n = \mathbf{g}(\mathbf{m}_n)$. Assuming a Gaussian travel time uncertainty, we can compute the solution to our problem through a linearized iterative inversion by which, at each step, we evaluate the next estimate of the model $\mathbf{m}_{n+1}$ by an update to the current model, $\mathbf{m}_n$, as:

$$
\begin{aligned}
\mathbf{m}_{n+1} = \mathbf{m}_n - \left(\mathbf{G}_n^T \mathbf{C}_D^{-1} \mathbf{G}_n + \mathbf{C}_M^{-1} \right)^{-1} \\
\left[\mathbf{G}_n^T \mathbf{C}_D^{-1} (\mathbf{d}_n - \mathbf{d}_{obs}) + \mathbf{C}_M^{-1} (\mathbf{m}_n - \mathbf{m}_{prior}) \right]
\end{aligned}
\tag{1}
$$

where $\mathbf{m}_{prior}$ is our a priori model, known with its covariance matrix $\mathbf{C}_M$; $\mathbf{d}_{obs}$ are the observed travel times, known with their covariance matrix $\mathbf{C}_D$; $\mathbf{G}_n$ is the matrix of partial derivatives approximating $\mathbf{g}(\mathbf{m}) \simeq \mathbf{G}_n \mathbf{m}$ near $\mathbf{m}_n$ [*Tarantola*, 2005].

[14] We simplify, assuming that:

$$
\mathbf{C}_M^{-1} = \left(\epsilon^2 / \sigma_D^2 I + \lambda^2 / \sigma_D^2 \mathbf{L}^T \mathbf{L} \right)
\tag{2}
$$

where **L** is the finite-difference expression of the Laplacian operator, so that parameters ϵ and λ, in turn, control vicinity of the model to the a priori one, and its smoothness [*Serretti and Morelli*, 2011]. We assume the error on measurements uniform and uncorrelated. Because of that the covariance matrix C_D is a diagonal matrix and can be written as $C_D = \sigma_D^2 I$.

[15] We use the LSQR algorithm [*Paige and Saunders*, 1982a, 1982b; *Nolet*, 1987; *Papazachos and Nolet*, 1997] to solve the linear systems as needed by equation (1).

[16] We choose to stop the iterative process after six iterations, when the data residuals have a variation by less than 1% with respect to the previous iteration. The "restraining" (ϵ) and "smoothing" (λ) parameters of the a priori model covariance matrix, chosen at each iteration are shown in Table 1. Notice that, as usually done in iterative optimization procedures [e.g., *Gill et al.*, 1982], we proceed with shorter steps during the first iterations, and release this condition only later on in the

Table 1. Restraining and Smoothing Factors Chosen at Each Iteration Based on Trade-Off Curves

Iteration Number	Restraining Factor ϵ	Smoothing Factor λ
1	400	300
2	300	300
3	250	200
4	200	200
5	150	100
6	100	100

process, to avoid instability. Figure 5 shows data misfit as a function of model norm variation for each iteration. Data misfit decreases, as model norm gradually increases, until convergence is reached.

[17] The tomographic model data misfit is also shown in Figure 4 (black curve) as a frequency histogram of seismic travel time residuals. We observe an RMS decreasing from 1.34 to 1.22 s with respect to the relocated residuals computed in the 3-D a priori model (red histogram), whereas the mean values remain stable. In the a priori model, the residuals larger than +2 s and smaller than −2 s are 18% of the total seismic rays number, whereas after the origin time relocation, they drop at 8.1%. In the final model, we still find some residuals larger than +2 s and smaller then −2 s, but they are only 6.5% of the total seismic rays number.

3. Synthetic Tests

[18] We perform synthetic tests to estimate the robustness of our inversion procedure. We attempt to reconstruct a 3-D structure by inverting a set of synthetic travel times computed for a known model, using the same distribution of sources and
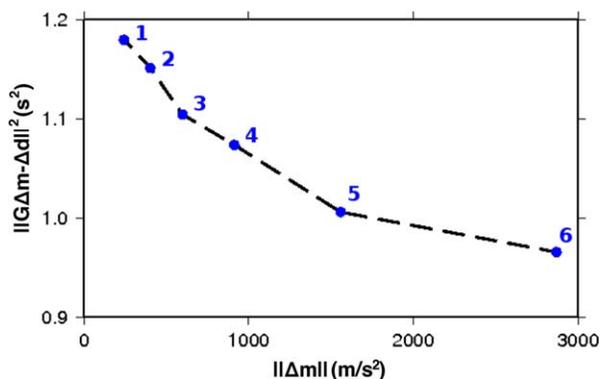

Figure 5. Data misfit as a function of model norm variation for each iteration (blue numbers). It has been normalized with respect to the number of seismic rays. Restraining and smoothing factors for each iteration are shown in Table 1.

stations as in the real case, and the same inversion procedure. Comparison between resulting and input models provides information on the ability and limitations of the inversion scheme to reconstruct real structure, and identifies regions with relatively better and worse performance. Such experiments are most often performed using an input model with a geometrical checkerboard pattern. We present in Figure 6, the results of such a test for three representative depths: 14, 18, and 28 km. The input model—Figure 6 (top left)—consists of an alternating 3-D pattern given by a sine-cubed function with period of 1.5° laterally, and 10 km in depth, overimposed on our a priori reference—EPcrust in the crustal region and sp6 in the mantle below. We add Gaussian noise to the synthetic travel times, with a standard deviation of 0.8 s to simulate the random data error. The anomalies
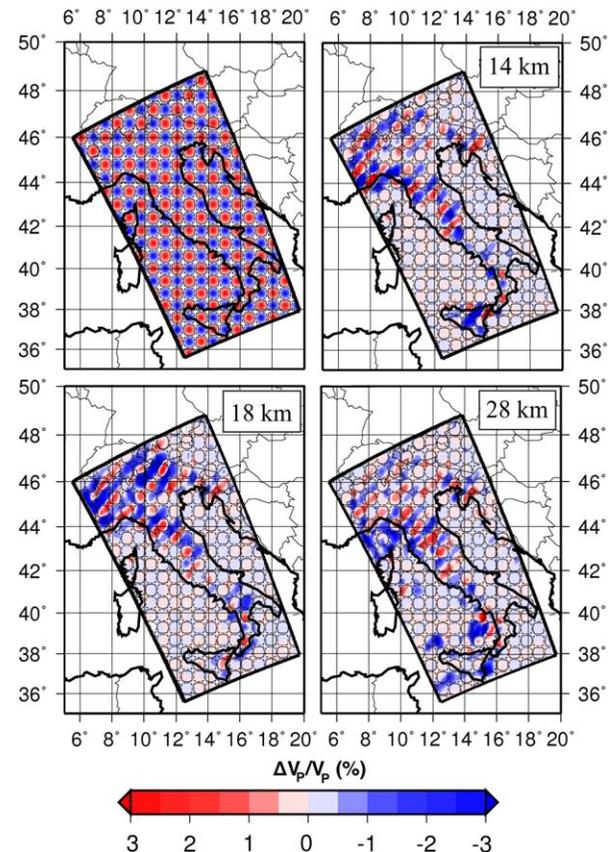
Figure 6. Resolution tests performed for synthetic structures as checkerboard test at three representative depths, 14, 18, and 28 km. The input model pattern is shown on the top left. We observe that we are able to reconstruct only the continental part of the studied area due to the stations-events distribution (Figure 2). Only the region inside the black rectangle is taken into account during the computation and it denotes the studied region.

are then plotted as relative velocity variations from the background model. As expected, in Figure 6 we observe that only the continental regions are well reconstructed. Because of the event and station distribution we miss the oceanic areas. In continental areas, this specific pattern of velocity is best reconstructed below the Alpine arc and North-central Apennines. There appears to be preferential NE-SO smearing, emphasizing an alignment of coherent velocity anomalies present in the input model, oriented diagonally with respect to the NS-aligned grid.

[19] We also note that the amplitudes of the anomalies are globally smaller than in the input model. This fact is commonly observed in these reconstruction tests, and hints at a general underestimation of wave velocity variations with respect to the background field. Besides, in Figure 6 it is also clear that positive and negative variations are not retrieved equally well. This may be ascribed to wave front healing, making the evolution in space of the time delay not symmetric with respect to the sign of the initial anomaly, with the signature of negative anomalies getting somehow obscured under some circumstances—even in the regime of validity of ray theory [*Wielandt*, 1987; *Nolet and Dahlen*, 2000; *Hung et al.*, 2001]. Our finite-difference forward calculation scheme correctly models the wave front healing effect—that may instead be neglected by more approximate ray tracing methods thus resulting in overly optimistic outcomes of synthetic tests. Our synthetic data set includes instead the healing effect in full.

[20] The real significance of this kind of tests has however been questioned. *Lévêque et al.* [1993] show, for instance, that under some circumstances small checkerboard patterns may be quite well imaged, even when larger-scale structure is much more poorly retrieved. Besides, in the nonlinear travel time inversion, raypaths—bent according to the wave speed model—assume quite unrealistic oscillating shapes [*Serretti and Morelli*, 2011]. For such reasons we deem better to use a more realistic model in a reconstruction experiment, with synthetic structures similar to what we expect to find. In this way, we can verify the capacity of the method to retrieve seismic velocity structures in a more realistic scenario. Figure 7 shows the input synthetic model on the left. The anomalies are plotted as relative velocity variations with respect to the background a priori model, consisting of EPcrust in the crustal region and *sp*6 in the mantle below. We build these shapes taking inspiration from the main geological and geophysical struc-
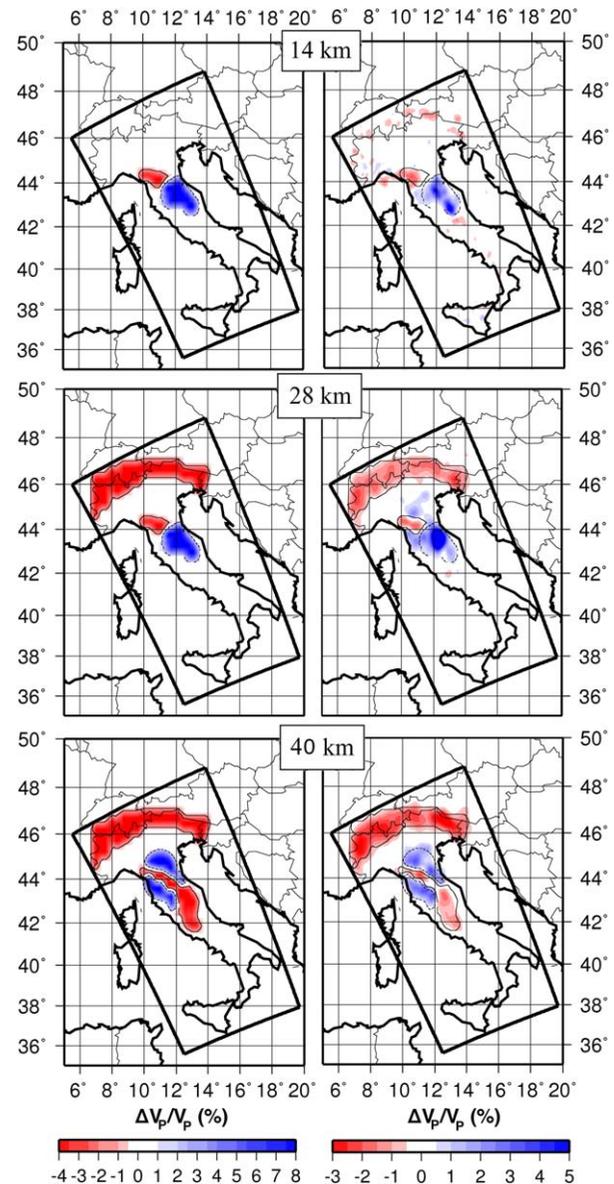

Figure 7. Synthetic test at three representative depths, 14, 28, and 40 km, one for each block of the a priori model. In fact, the synthetic input model has been built considering three ranges of depth having three different anomalous blocks, from 10 to 18 km, from 20 to 28 km, and from 30 to 48 km. (left) The synthetic input model and (right) the reconstructed one. Only the region inside the black rectangle is taken into account during the computation and it denotes the studied region. We use a smaller scale range for plotting the reconstructed model with respect to the synthetic input one.

tures present in the peninsula, as described in the literature. We divided the input synthetic model in three sectors as a function of depth, where we superimpose different heterogeneous shapes to the background a priori model. Figure 7 (left) shows the structure at three representative depths, one for each of the different sectors of the input model. As
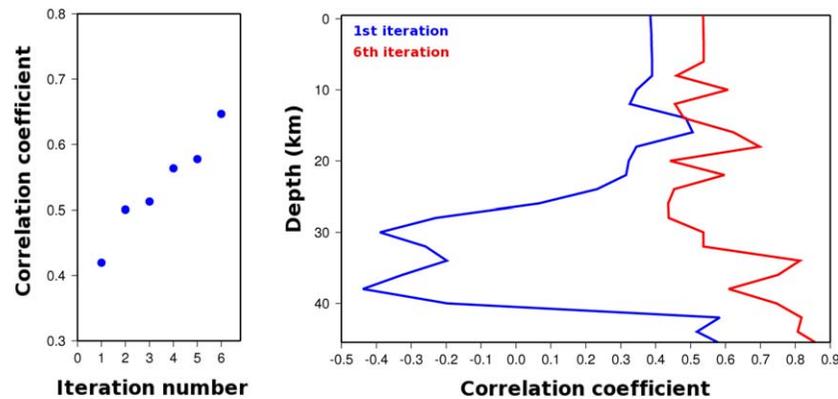
Figure 8. (left) Average correlation coefficient for each iteration. We observe an increase of the correlation coefficient of about 35%, from 0.42 until 0.65. (right) Correlation coefficient as a function of depth after the first (blue) and the last (red) iteration. We can observe that, after six iterations, the correlation coefficient increases particularly in depth, where the ray coverage increases (compare with Figure 3).

before, for this synthetic model we calculate synthetic travel times along the paths in the real data set. To simulate the random error present in the real data, we added Gaussian noise to the synthetic travel times with standard deviation of 0.8 s. As we observed for the checkerboard test, the intensity of anomalies in the reconstructed model (right) is underestimated with respect to the input model (left). This observation will bring some contribution to the discussion on the final tomographic model (see next section). Figure 7 (top) shows a horizontal cross section at 14 km depth, representative of the input model in the range from 10 to 18 km. The synthetic pattern shows the alternation of positive and negative anomalies, simulating geological structure in the shallow part of the crust. The reconstructed model, to the right, shows good agreement in spatial shape along the Apennines. The intensity of anomalies is generally lower than in the input model. The reconstructed model also presents some background noise—with anomalies smaller than 1%—along the Apennines and especially along the Alps, in regions where the input model has $\Delta v_P/v_P = 0\%$. This tendency is due to the fact that, in the input model, few kilometers below, the second model sector presents negative anomalies along the Alpine chain. The middle row of Figure 7 shows, to the left, the input model cut at 28 km. In this depth range (from 20 to 28 km) we include a low velocity body to represent the Alpine roots. The outcome of the reconstruction test is good below the Northern Apennines and the Alpine Arc in terms of shape of the anomalies, although the amplitude is, again, underestimated. We may expect that the retrieved intensity of seismic velocity heterogeneity will

also be affected by this underestimation. As in the previous layer, scattered small-amplitude positive anomalies are present along the Apennines. These anomalies are related to the third sector of the input model, beginning just below this 28 km depth. On the other hand, at 40 km depth—representative of the depth interval in the input model between 30 and 48 km—both the Alps and the Apennines are quite well retrieved in shape (see Figure 7), whereas the anomalies are underestimated in intensity.

[21] To evaluate quantitatively the resemblance between output and input models, we compute the correlation coefficient between the two fields. It reaches the value of 65% after six iterations, as shown in Figure 8 (left). Figure 8 also shows the correlation as a function of depth for the first and the last iteration. Note that some relatively worse correlation—between, say, 20 and 30 km—could have been expected as it roughly corresponds to a notch in the ray density (Figure 3). The relative data misfit between travel times calculated in the final model and in the synthetic model decreases by 20% after six iterations, as shown in Figure 9. The misfit reduction is comparable with the data misfit decrease in the tomographic model (Figure 5). At each step the relative data misfit decreases less and less, reaching convergence after six iterations. A seventh iteration would produce a decrease in data misfit by less than 1%.

[22] The correlation between output and input models in Figure 8 is rather high in the depth span typical of the crust-to-mantle transition, due to the good sampling provided by rays in our data set (Figure 3b). We expect to retrieve the velocity
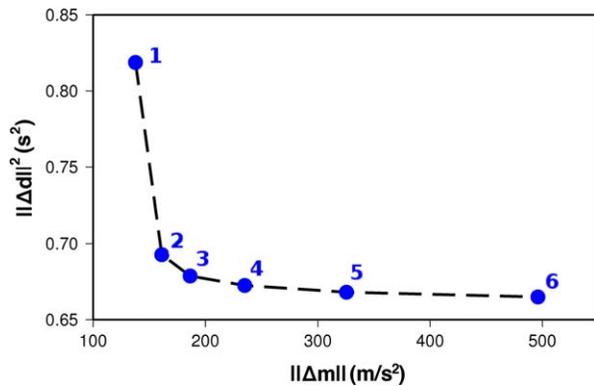
Figure 9. Synthetic relative data misfit, $\| \Delta d \|^2$, as a function of the norm of the model for the six iterations performed (blue numbers). It has been normalized with respect to the number of seismic rays. Data misfit decreases of about 20%, a value comparable with data misfit decreasing of the tomographic model (Figure 5). The initial data misfit results dominated by the Gaussian error we added to the input model, having a variance of 0.64 s². Restraining and smoothing factors are shown in Table 1 for each iteration.

structure particularly well in this vertical range, so that, although we do not explicitly honor this transition as a discontinuity, we may think to search for a Moho as the locus of points where wave velocity transitions from crustal to mantle values. Figure 10 shows the simulated reconstruction of such a Moho, for the input model (top) and for the reconstructed model (bottom). Deepening of the transition, down to 60 km, is well reconstructed, such as a shallowing of this model Moho—whose extent appears instead under-estimated by some 5–7 km. The positive outcome of this further test induces us to use this criterium to the Moho in the model resulting from inversion of real data.

4. Results

[23] In this section, we present the results of the nonlinear tomographic inversion, as a new velocity model, contributing some interpretation in terms of the geological structures that we may recognize in the maps. We also seize this opportunity to provide a general view of the current state of knowledge about the structure of the crust and uppermost mantle in the Italian region. An animation showing maps of the model, as the depth sweeps from the surface to the bottom of the model, is provided as supporting information.[1] Here we focus our attention on selected horizontal

and vertical sections that show the main features of the reconstructed three-dimensional *P* wave velocity field.

[24] Figures 11 and 12 illustrate our resulting tomographic model (right) compared with the a priori model (left) at selected depths in terms of absolute velocity. These depth sections represent the whole model quite completely, given some vertical continuity, as shown by the vertical cross sections described further on. The layered 3-D reference model EPcrust [*Molinari and Morelli*, 2011], that we use as our a priori crustal model, has laterally varying interface depths separating upper from lower crust, and an undulated Moho discontinuity with the mantle. Seismic velocity assumes rather different values going from uppermost crust to mantle, so that to represent subtle

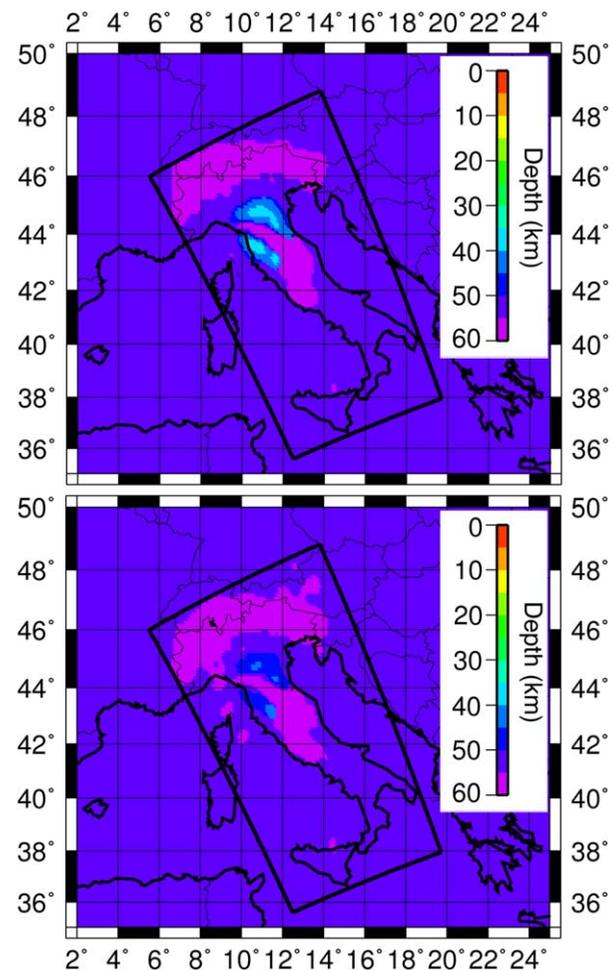**Figure 10.** Simulated reconstruction of crust-mantle transition in the synthetic test, defined as depth of exceedance of a threshold wave speed. (This criterium will be used further on to define a reconstructed Moho for the inversion of real data.) (top) Interface in the input model. (bottom) Interface deduced from the reconstructed model.

---

[1]Additional supporting information may be found in the online version of this article.
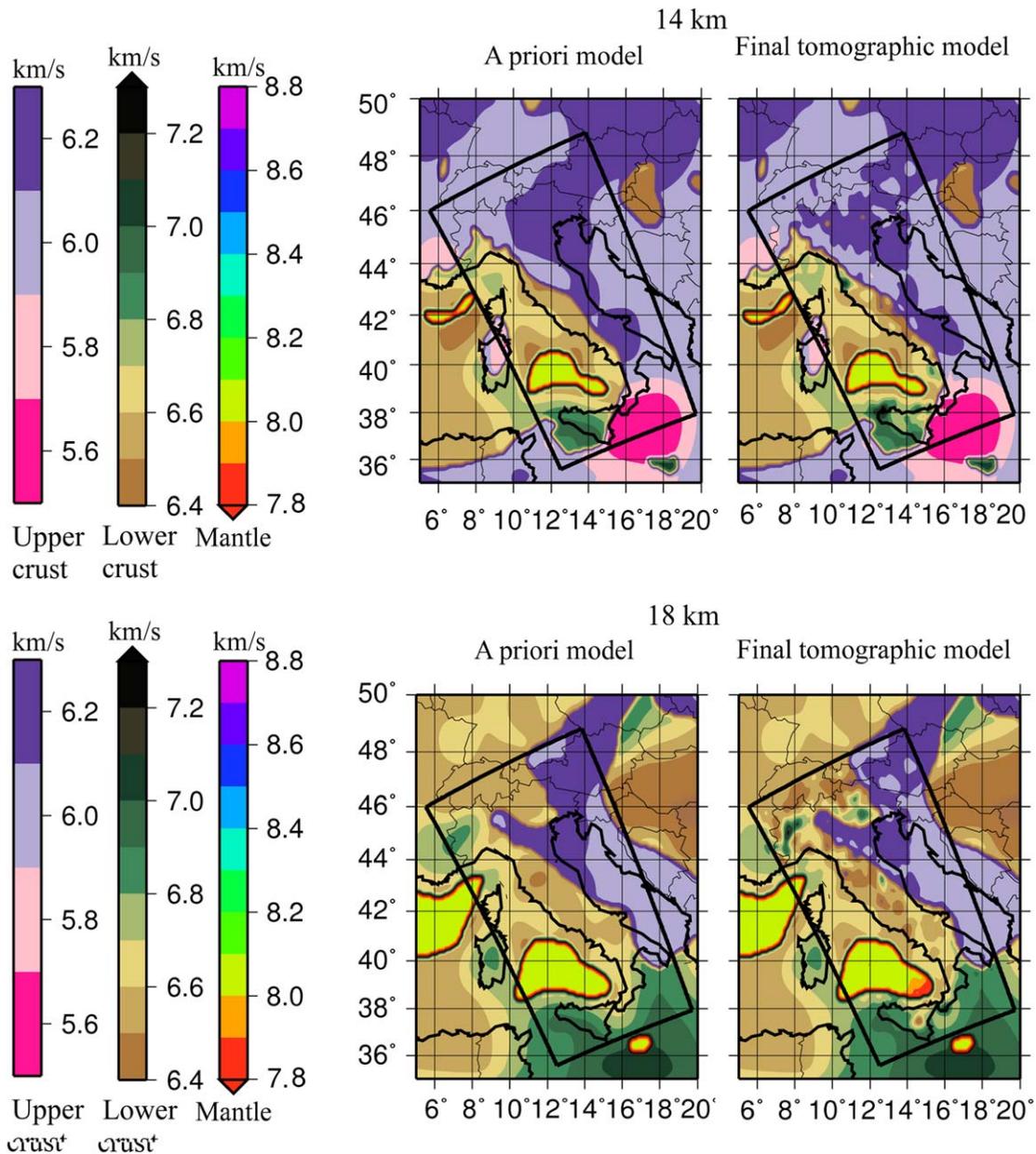
Figure 11. (left) A priori model and (right) tomographic images at 14 and 18 km in terms of absolute *P* wave velocity. We represent the main parts of the a priori model—lower crust, upper crust and mantle—by using three different color scales. Starting from the left, we use colors from pink to violet for the upper crust, from brown to black for the lower crust and from red to magenta for the mantle. Only the region inside the black rectangle is taken into account during the computation and it denotes the studied region.

velocity variations we use three different color scales for velocity values pertaining to these three domains. We use colors varying from pink to violet for the upper crustal velocity range, from brown to green-black for lower crustal velocity, and from red to blue-magenta for the mantle.

[25] The first map in Figure 11 is cut at a constant depth of 14 km. At this depth the Apennines

roughly follow the boundary between upper and lower crustal material. Slower upper crust, to the East, is denoted by violet, and it is relative to *P* velocity values from 5.9 to 6.3 km/s. Following *Di Stefano et al.* [2009], we may note that in the upper crust *P* wave velocity patterns reflect local geology: highs correspond to limestone or crystalline basement units, and lows to recent sedimentary basins. In our case, this behavior is to some
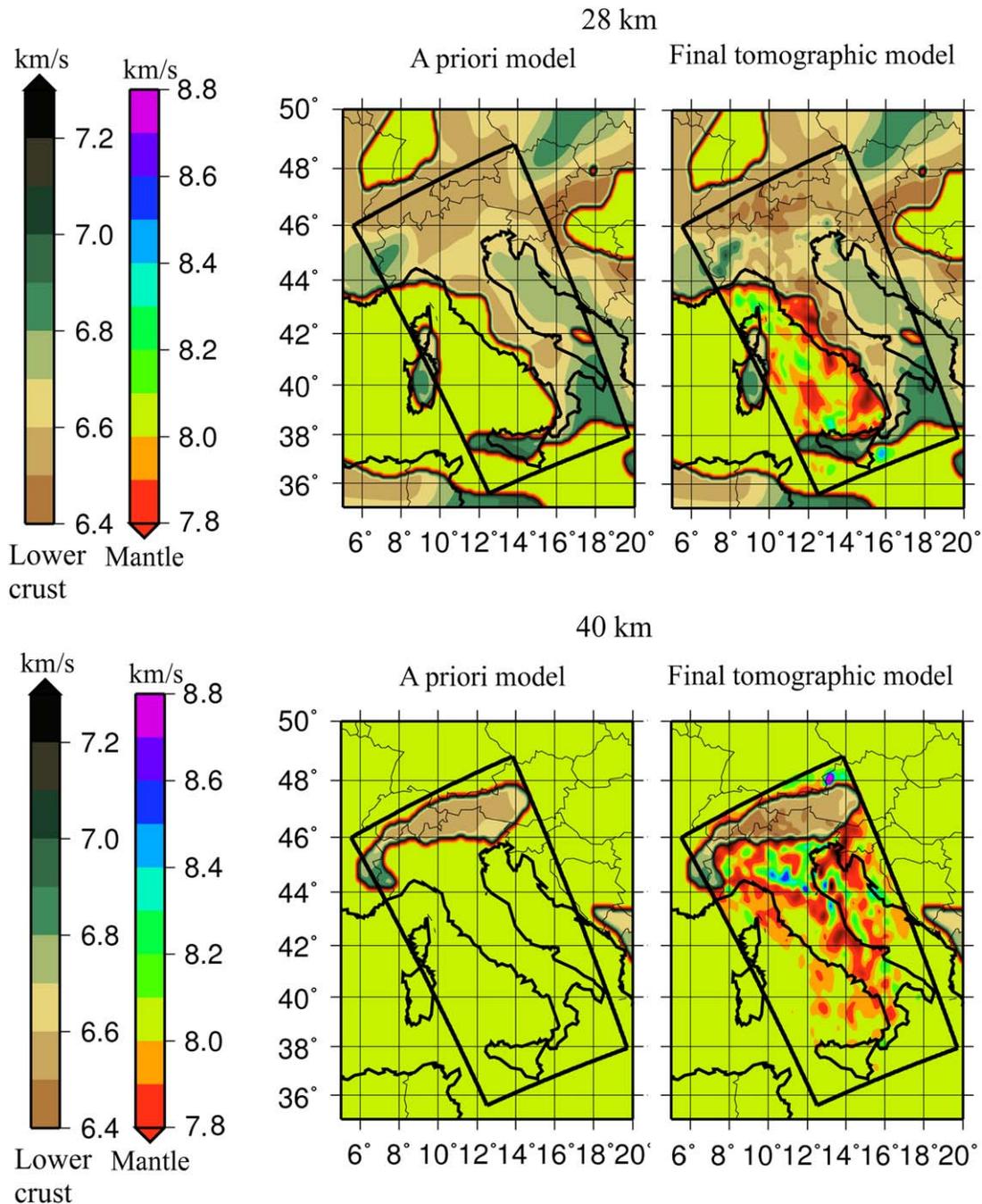
Figure 12. (left) A priori model and (right) tomographic images at 28 and 40 km in terms of absolute *P* wave velocity. We represent the main parts of the a priori model—lower crust and mantle—by using two different color scales. Starting from the left, we use colors from brown to black for the lower crust and from red to magenta for the mantle. Only the region inside the black rectangle is taken into account during the computation and it denotes the studied region.

extent inherited from EPcrust [*Molinari and Morelli*, 2011]. Lower crustal anomalies—shown with a brown-black color scale—are instead relative to values from 6.4 up to 7 km/s in the a priori model and up to 7.3 km/s in the tomographic model. Mantle material is present at the center of the Tyr-

rhenian Sea, in correspondence of the magmatic area of the volcanic arc of the Eolian Islands and the Marsili Seamount—see Figure 1 for toponyms. Melted mantle is believed to rise in the lower crust in the southern Tyrrhenian Sea, above the steeply dipping Ionian, feeding the magmatism of the

volcanic arc of the Marsili Seamount. Its basin is near circular in shape, with a diameter of about 120 km, in accordance with *Marani and Trua* [2002]. The presence of mantle is quite limited at this depth. Typical mantle velocities are geographically quite localized, mostly slow in a relative sense, with velocities around 8 km/s both in the a priori and the final model (the structure under the Tyrrhenian Sea is not well retrieved because of scarce ray coverage, as shown in section 3). Following the Apennines Arc, we may observe that in the northern part of the Apennines the border between these two types of crustal material is moving to the west with respect to the a priori model. We observe in general that the anomalies have the tendency to become less smooth, which is a typical behavior for a tomographic model with respect to a simpler a priori reference. A small slow anomaly appears in the final tomographic model under the Etna volcano area and it may be related to its crustal roots.

[26] The second plot in Figure 11 maps the model at 18 km depth. Compared to the shallower depth, we now observe a considerable decrease of the upper crustal domain. Along the Apennines we find quite isolate slow anomalies (dark violet and dark brown) which follow the mountain belt. On the contrary, *Di Stefano et al.* [2011] have shown at 22 km depth a quite continuous slow anomaly. The mantle under the Tyrrhenian is wider (light green, orange, and red areas) than at 14 km depth. Mantle velocities are 8.03 km/s in the a priori model, but become slower after inversions in the area of Eolian Island and Marsili volcano. Velocity values close to 7.8 km/s or slightly lower—absent in the a priori reference, as quite unrealistic both for crustal and for mantle rocks—may result from the inversion lowering a starting mantle velocity of, say, ∼8 km/s. In view of the tendency to underestimate adjustments to the initial model, quite usual in tomographic inversions and also suggested by results of the synthetic model reconstruction tests shown in section 3, we interpret such features as the actual detection of crustal rocks. As our model representation—a continuous interpolation among nodes of a 3-D mesh, described in section 2—does not impose an explicit Moho, it may induce some smoothing of the crust/mantle border as a result of inversion. However, a sharp transition from typically crustal to mantle velocities is generally present. The Etna volcano area diverts form the a priori model showing a slow velocity patch shifted toward the south with respect to 14 km depth. In the final tomo-

graphic model, the central and eastern part of the Alps are characterized by low velocity roots (in dark brown and light violet), in agreement with previous tomographic studies such as *Alessandrini et al.* [1995], *Chiarabba and Amato* [1996], *Waldhauser et al.* [2002], and *Di Stefano et al.* [1999, 2009], whereas the a priori model shows two blocks of uniform upper and lower crust velocities. This fact may mean that the Alpine region at 18 km depth is mostly characterized by typical upper crustal rocks that underthrust the mountain belts [*Di Stefano et al.*, 2009]. In the Eastern Alps, the relationship between the European and Adriatic plates is controversial [e.g., *Lippitsch et al.*, 2003; *Schmid et al.*, 2005]. Results from migrated receiver functions [*Kummerow et al.*, 2004] suggest that the European Moho underthrusts the Adriatic lithosphere to the south. On the other hand, *Lippitsch et al.* [2003] and *Schmid et al.* [2005] assert that a high-velocity body connected to the Adriatic lithosphere is subducting northeast beneath the European plate. At the western part of the Alpine arc, a lithospheric unit, known as the "Ivrea body", has been recognized as consisting of peridotitic rocks with high seismic velocity and density—typical of lower crust and mantle—at shallow depth and surrounded by crustal material [e.g., *Schmid and Kissling*, 2000]. In Figure 11 at 18 km depth, the high velocities (in green-black) below the western part of the Alps are then related to this Ivrea body [e.g., *Solarino et al.*, 1997; *Schmid and Kissling*, 2000; *Diehl et al.*, 2009; *Wagner et al.*, 2012]. A fast anomaly was already present in the a priori model at this depth, but its amplitude, shape, and geographical location have been completely reshaped in the final tomographic model. In Figure 13, we show a vertical cross section under the western Alps plotting relative velocity changes with respect to the a priori model. The figure shows then the update improvement to the reference crustal model due to our inversion. In spite of a varying amplitude—likely reflecting the seismic ray density—it is clear the presence of a continuous high-velocity body between about 15 and 40 km depth, with some discontinuous fast anomalies above and below it. This fast seismic anomaly in the lower crust is inconsistent with common velocity of crustal materials [*Christensen and Mooney*, 1995], and it is more consistent with the typical mantle velocity. The Ivrea body finds an explanation as a piece of rising mantle that forms the rigid frontal part of the Adriatic plate [*Schmid and Kissling*, 2000; *Schmid et al.*, 2005]. The high-velocity anomaly in Figure 13 is in general agreement with previously proposed models
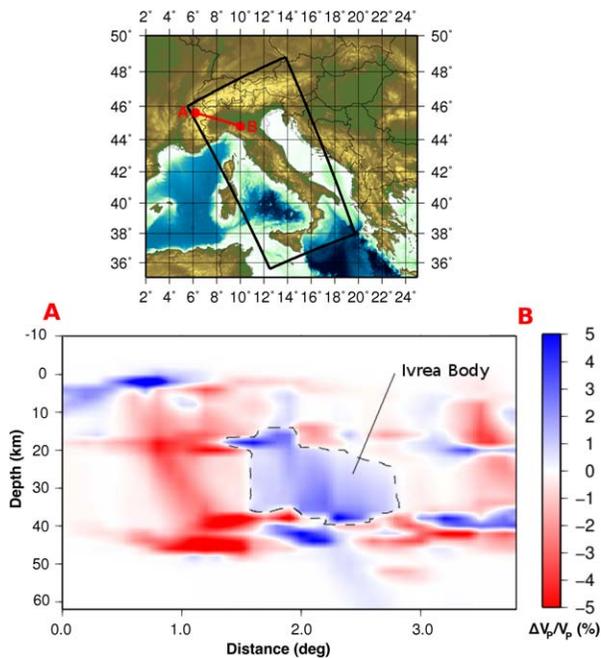
Figure 13. Relative velocity change, with respect to the a priori model, along a vertical cross section under the Western Alps. We find a wide high velocity anomaly positioned between 20 and 40 km. We hypothesize that it is related to the Ivrea-Verbano body.

of the Ivrea body, based on deep seismic sounding data [e.g., *Solarino et al.*, 1997; *Schmid and Kissling*, 2000; *Diehl et al.*, 2009; *Wagner et al.*, 2012] both in terms of location and vertical extension of the anomaly. Because of our irregular seismic ray coverage, we are not able to detect the Ivrea body deeper than 40 km and shallower than 15 km, whereas *Solarino et al.* [1997] claim that the body extends from 2 to 62 km depth.

[27] Figure 12 shows deeper layers, at 28 and 40 km. Here the upper crust disappears. Lower crust and mantle can easily be distinguished as they are presented with two different color scales, from brown to black and from red to magenta, respectively. At 28 km depth, we note quite a sharp edge running along the Apennines, where both the crustal region, to the East, and the mantle, to the West, are marked by slow anomalies. The continuous slow anomalies—which were not present in the a priori model—along all the Tyrrhenian coast are probably related to strong thermal activities indicating asthenosphere upwellings [*Di Stefano et al.*, 2009]. This hypothesis is also supported by a concentration of very high attenuation in the Tyrrhenian wedge, above the Adriatic subduction slab, as explained by *Piccinini et al.* [2010]. The narrow slow anomalies extend along all the Tyr-

rhenum side of the Apennines, marking the roots of Quaternary volcanoes and the magmatic provinces of Tuscany, Latium, Campania, and the Aeolian Islands. This low-Vp anomaly hence correlates with Quaternary volcanoes and geothermal activity. We may thus interpret these features as due to thermal anomalies, in agreement with the observed high heat flow [see *Di Stefano et al.*, 2009, and references therein). The hypothesized thermal state reconciles with the ending of magmatic activity in this area at about 0.3 Ma [*Piccinini et al.*, 2010]. In the Western Alpine region at this depth, we note that the absolute velocity moves from a maximum velocity of 6.8 km/s in the a priori model to a maximum velocity of 7.0 km/s in the final tomographic model. We believe that this tendency to retrieve high velocities in this region is associated with the Ivrea-Verbano body. *Wagner et al.* [2012] identify the Ivrea-Verbano body at 28 km depth (their Figure 5) with comparable *P* wave velocities. The Ivrea-Verbano body, which was already present in the a priori model at 28 km as a piece of high crustal velocity, has been completely reshaped after the inversion process by the new data set, like at 18 km depth (Figures 11 and 13). In the central part of the Alps, we note slow anomalies—which are not present in the a priori model—mainly associated with the crustal root of the Alps, in substantial accord with *Diehl et al.* [2009].

[28] At 40 km depth (Figure 12) besides clear crustal "roots" under the Alps already seen in the a priori model, we mostly observe the presence of mantle rocks. However, a main trait in the final tomographic model is given by the slow anomaly continuously running below the entire Apennines crest. This feature is not present in the reference model, that at this depth consists of laterally uniform mantle. We may interpret it as crustal material, as the velocity is too low for mantle rocks. Such explanation is indeed in agreement with seismic receiver functions [e.g., *Piana Agostinetti et al.*, 2008; *Piana Agostinetti and Amato*, 2009; *Bianchi et al.*, 2010] and gravity studies [e.g., *Tiberti et al.*, 2005]. In the following section, we discuss this interpretation, involving deepening of the Moho, in more detail. Low seismic velocities at this depth may also have different origin. Continental crustal material in subduction zones may be carried down by the Adriatic lithospheric slab [e.g., *Di Stefano et al.*, 1999, and references therein]. Mantle seismic anomalies can also be associated with thermal effects. In this case, the deep slow Apenninic anomaly could be associated

with rising hot asthenospheric material in front of the Adriatic slab. Several evidences have been found by *Mele et al.* [1998], *Di Stefano et al.* [1999], *Piromallo and Morelli* [1997], and *Piromallo and Morelli* [2003]. In the Alpine region, we see the presence of lower crustal material, mostly slower than the a priori model, and then much slower than the Apenninic anomaly. Both the features found beneath Alps and Apennines confirm previous studies about the existence of crustal roots nd the presence of a deep Moho in these areas [e.g., *Piana Agostinetti and Amato*, 2009, for the Apennines Moho; e.g., *Stehly et al.*, 2009, for the Alps Moho].

4.1. Moho Depth

[29] Figure 14 shows three vertical, parallel, cross sections cut through the a priori model (left) and the final tomographic model (right) roughly orthogonally with respect to the axis of the Apennines. We notice that the crust/mantle discontinuity in the a priori model is understandably smoothed out in the tomographic result that has no constraint imposed on the velocity field. However, a sharp transition is still recognizable that can be associated to the Moho and that is entirely required by travel time data. This Moho remains shallower at the Tyrrhenian side, about 20 km, than under the Adriatic, about 40 km, and is deepest under the Apennines, where it reaches about 40 km. Notice a clear indication of increased depth of the crust/mantle transition with respect to the initial model. Cross sections AB and CD show indications of deepening of the Adriatic Moho toward SW, consistent with models of lithospheric subduction and receiver function studies [e.g., *Piana Agostinetti et al.*, 2008; *Piana Agostinetti and Amato*, 2009; *Bianchi et al.*, 2010] that also show a SW-dipping Moho and a flat ∼20 km thick Tyrrhenian crust. The deepest Moho along the Apennines—46 km—is reached in section EF, in correspondence to the highest mountains.

[30] Moho topography is strongly correlated with tectonics and geodynamic processes and strongly influences the measure of most of the geophysical properties of the Earth, like the gravity field and the propagation of seismic rays. Hence a detailed Moho map is a key requisite for geodynamic modeling, for understanding the evolution and state of lithosphere, and to correct seismic data to map the upper mantle structure [*Lippitsch et al.*, 2003]. A first-order discontinuity is not present in the tomographic model, but the sharp transition

from typical crustal to mantle *P* wave velocity appears to be a reliable way to identify the Moho. We can therefore search the sudden transition from 7.6 to 8.0 km/s in our model, and map its depth over all the region. Figure 15 shows the map of this Moho depth, compared with the a priori model EPcrust [*Molinari and Morelli*, 2011]. The geographical area covered in this paper is marked by a black rectangle. Outside this area, the Moho depth does not change with respect to the a priori model. The total range has not changed considerably after the inversion, going from 10 to 50 km in the a priori model, and reaching 52 km in the final model, compatibly with receiver function studies [e.g., *Piana Agostinetti and Amato*, 2009; *Di Stefano et al.*, 2011]. However, we can point out some significant improvement in the final model. The most noticeable variation is under the main reliefs, i.e., Alps and Apennines. The deepest Alpine area is wider in our Moho model than in EPcrust. In particular, the deep eastern area is wider both in latitude and longitude, and is also deeper.

[31] Indeed, in this area, the purple-colored area is broader than in the top figure, indicating depths down to 52 km. The western area, under the French-Italian border close to the Ivrea zone, shows depth down to about 50 km. These features are in agreement with other studies concerning this area—e.g., from inversion of seismic ambient noise [*Stehly et al.*, 2009], and from wide-angle seismic tomography [*Bleibinhaus and Gebrande*, 2005]. Making a comparison between Figure 15 and the topography map we can easily observe that our Moho depth follows the topographic elevation in the Alpine region. It is clear that the Moho depth, at a first order, qualitatively accounts for isostatic equilibrium. In the western part of the Alps, we obtain Moho depths shallower by about 10 km than some regional studies, such as *Wagner et al.* [2012]. The Alpine roots show here a quite continuous trend. On the contrary, *Di Stefano et al.* [2011] present a discontinuity around 46° of latitude and 8° of longitude, with depths about 10 km shallower than in our case.

[32] To the South of the Alpine chain, the border between the Alps roots and the Po Plain region is clearly marked out. The crustal thickness reaches about 30–35 km. This is the signature of the plate boundary between the European plate, to the north, and the Adriatic plate. The boundaries of these plates correlate with the strike of the Eastern Alps and the Dinarides. The European Moho dips to the south and the Adriatic Moho dips to the

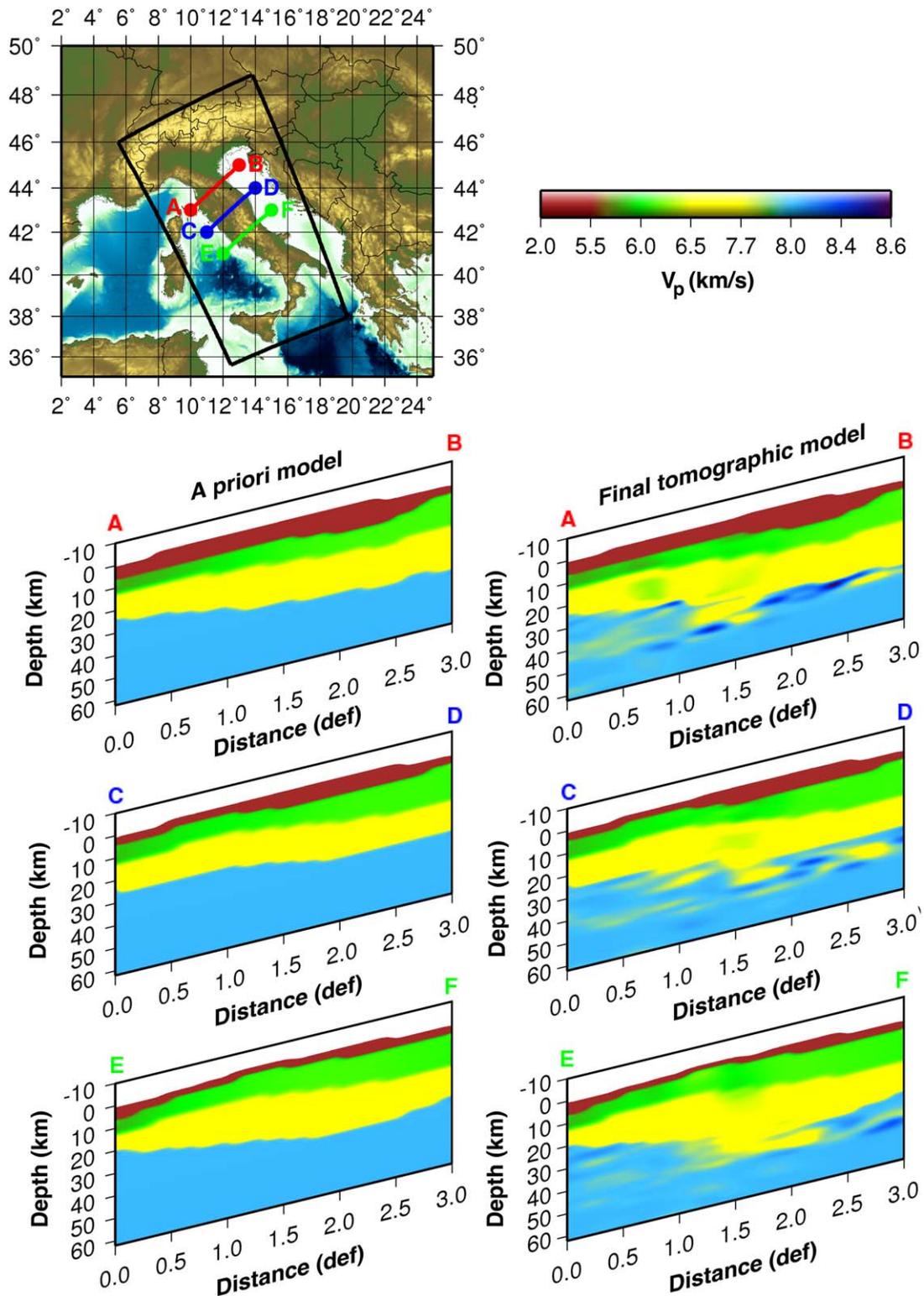**Figure 14.** Three parallel vertical cross sections cut along the Northern Apennines. (left) The a priori model and (right) the final tomographic model. In the central part of all three sections, moving from North to South (from AB to EF), we find out that the deepest part of the Moho moves toward the East. The Moho depth is marked by a sharp transition between yellow (lower crust) and blue (mantle).
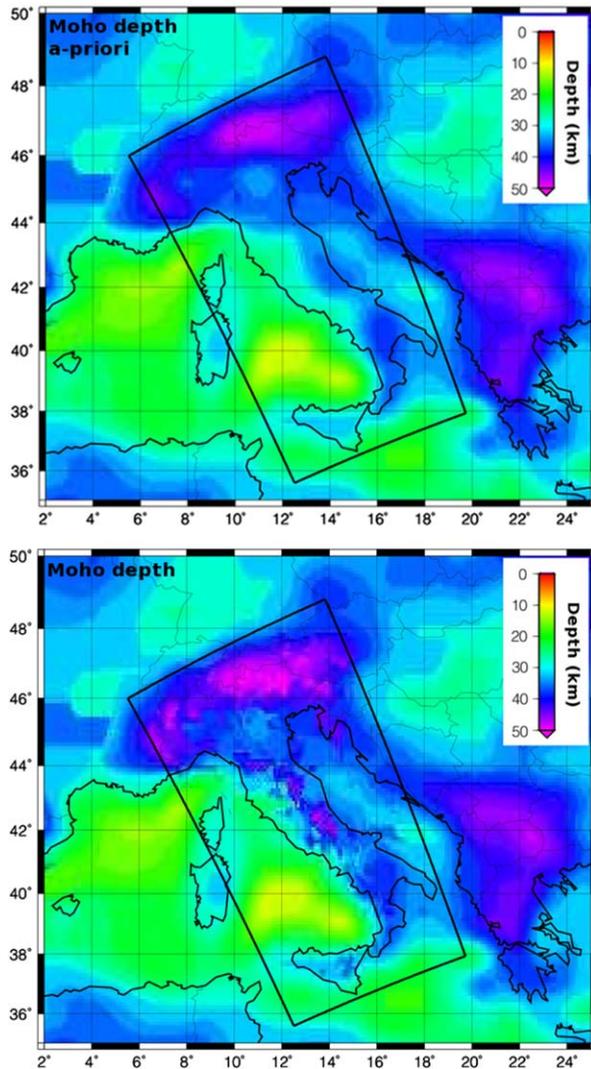
Figure 15. (top) Moho depth in the a priori model. (bottom) Moho depth identified as a sudden transition from 7.6 to 8.0 km/s in the final model. The studied area in this paper is inside the black rectangle. Outside the Moho depth is the same as in the a priori model. We observe a deeping Moho especially under the central Apennines and the Western Alps. Only the region inside the black rectangle is taken into account during the computation and it denotes the studied region.

north-east. The imprint of the Po plain on the Moho topography is partially inherited from EPcrust [*Molinari and Morelli*, 2011], but it appears shallower for a wider area.

[33] Another important peculiarity of our Moho depth is along the Apennines chain, where its structure significantly differs from the a priori information. In the same way as for the Alpine belt, here we can observe an arc of deeper Moho along the Apennines. It reaches depths just short

of 50 km only in three main areas located under the Northern and Central Apennines. The discontinuity of the Moho depth under the Apennine Chain has been recognized by previous studies, e.g., the teleseismic receiver function study by *Piana Agostinetti and Amato* [2009]. This feature suggests a discontinuity of the belt axes in central southern Italy, between 41° and 42° [*Amato et al.*, 1993; *Piromallo and Morelli*, 2003; *Di Stefano et al.*, 2011]. We can also point out the largest Moho depth under the Gran Sasso area (about 46 km depth) in Central Italy. This Moho deepening has also been found by *Piana Agostinetti et al.* [2009]. We observe that the sharp boundary steepness of the Adriatic plate approximately decreases from north to south, as pointed out by *Di Stefano et al.* [2009]. The Apennines belt continues the South in the Calabrian Region, where we do not observe any significant changes with respect to EPcrust. The Calabrian Arc is characterised by Moho depth around 40 km, like in *Di Stefano et al.* [2011]. We believe that this lack of variation of the Moho depth in the Calabrian region may be mostly due to the poor path coverage of our data set in this area. We detect instead an increase of the thickness of the crust under the Etna area, increasing from about 30 to 35 km. On the northeast of the Apennines chain, the Ligurian Moho changes in depth from a about 20 km beneath the deepest parts of the Ligurian Sea—see Figure 1 for toponyms—to about 30 km beneath the mountain chain. This evidence is in accord with the result of the regional study developed by *Wagner et al.* [2012], despite of their border is shifted toward the north and it is better constrained. All the Tyrrhenian side of the Apennines (i.e., Tuscany, Latium, and Campania) is characterized by shallow depths, with consistent values between 20 and 30 km, in accord with results shown by *Piana Agostinetti et al.* [2009] and assert by *Wagner et al.* [2012].

[34] A Moho depth minimum, around 10 km depth, is imaged in the central Tyrrhenian sea, where the Seamount Marsili is located. Despite of we observe some Vp velocity anomalies in this area (see Figure 10, 18 km depth), the Moho map does not show significative additional anomalies. These Moho depths presented by EPcrust are in substantial accord with *Di Stefano et al*. [2011].

5. Conclusions

[35] In this paper, we present a new model for the *P* wave velocity structure of the Earth's crust and

uppermost mantle beneath Italy, derived by seismic travel time tomography with an innovative implementation consisting of full 3-D finite-difference forward calculation and nonlinear iterative inversion of first-arrival travel times between earthquakes and stations located in the study region (Figure 2). The finite-difference method used for forward calculations [*Podvin and Lecompte*, 1991; *Tryggvason and Bergman*, 2006] is able to tackle strong heterogeneities and discontinuities, such as those present in the crust. Although computationally more expensive, tracking the full wave front through the 3-D medium avoids inaccuracies and difficulties met by approximate or iterative ray tracing schemes, such as ray bending methods that may not converge to true minimum-time paths [*Serretti and Morelli*, 2011]. This is particularly relevant for a strongly heterogeneous setting, such as that encountered in crustal tomography that include modeling of the Moho. Coupled to this numerical scheme to solve the forward problem, we implement a nonlinear iterative inversion method that uses full 3-D a priori in the form of a reference crustal model, and permits stable inversion with a detailed model description.

[36] The resulting model provides a local improvement of the recent 3-D crustal reference model EPcrust [*Molinari and Morelli*, 2011], that we use as a priori information in the inversion. Although the model is represented by absolute *P* wave velocity on a 3-D grid of nodes, and it does not explicitly include any discontinuity, a reliable estimate of the crust-mantle boundary can be obtained mapping the strong gradient marking the transition from typical crustal velocity values to mantle ones. The resulting map of Moho depth reveals some significant features, and—as it is not induced by any explicit parameterization—it can be considered an unbiased estimate of crustal thickness.

[37] The resolution of the model strongly depends on the coverage of seismic rays. Given the limited areal extent of the model, and our choice of using only stations and hypocenters located inside the study region, first-arrival seismic rays only dip down to about 60 km, but fair coverage is limited to the first, say, 50 km. The synthetic model recovery test (Figure 7) however shows good capability of reproducing velocity structures, particularly for layers and areas with good ray coverage. Adequate presence of seismic stations is essential to guarantee good seismic ray illumination—and hence reliable tomographic images—in the shallower layers of the crust. The scarcity of seismic stations in the

Po Plain area does not permit here to update the prior model with lateral variations of seismic wave velocity.

[38] The main velocity heterogeneities recovered by this work can be related to geological evidences on the shallower part of the crust, and to geophysical processes in the deeper one. Starting from a depth of about 18 km we see a low velocity area—laterally discontinuous in the shallow part, but much more continuous deeper down—beneath the Alpine and Apenninic belt, likely related to plate subduction processes [*Carminati and Doglioni*, 2012] or delamination [*Benoit et al.*, 2011]. We confirm the presence of the Ivrea body, a high-velocity body which is not consistent with properties of known crustal rocks, but is rather assimilated to mantle material surrounded by crust. We have found the Ivrea body extending from 15 to 40 km, in agreement with previous studies [e.g., *Schmid and Kissling*, 2000; *Schmid et al.*, 2005; *Nicolich*, 2010].

[39] We also present a new map of the Moho topography for the Italian region, obtained considering the velocity transition from 7.6 to 8.0 km/s retrieved in the final velocity model as the transition from the crust to the mantle. The map shows a shallower Moho on the Tyrrenian side, with about 20 km, becoming deeper beneath the Apennines chain, to about 40 km. The Adriatic side presents a Moho depth at about 30 km. The deepening of the Moho surface under the mountains belt, which corresponds to the low-velocity arc present in the tomographic images, is due to the presence of isostatically compensated mountains roots. In the western part of the Alps we observe deepening of the mountain roots that reach about 50 km in correspondence of the Ivrea body. The border between the roots of the Alps and the Po Plain region is well marked after the inversion. The Moho depth is about 30–35 km under the Po Plain and around 50 km in the Alpine region. Along the Apennines, the map shows the presence of a deep Moho arc, which marks the belt trend. It reaches a maximum depth of about 50 km only in three areas located under the Northern and Central Apennines. This maximum depth is in general comparable with the Alpine Moho, except for the Western Alps which record the deepest Moho area in Italy. These considerations are in agreement with previous studies obtained using receiver functions [e.g., *Piana Agostinetti and Amato*, 2009; *Di Stefano et al.*, 2011]. We note that, although regional-distance first-arrival travel times are generally not deemed the most appropriate data set to map

Moho depth, and in spite of the fact that no discontinuity is prebuilt in the model parameterization, by accurately modeling wave front propagation our method is indeed able to retrieve the crust/mantle boundary in a geographically extensive region with good confidence.

[40] The quality of any tomographic model depends on an accurate method and on the virtues of the data set. The performance of our method has been extensively documented in the paper, and is also validated by the results, but we have also commented on some limits posed by the data set. We have considered *P* wave travel times retrieved from the high-quality EHB Bulletin of the International Seismological Centre [*ISC*, 2009] for the time period between 1988 and 2007, but some improvement may in fact be possible. First of all, the apparent gap in station coverage in Northern Italy is currently being filled by new seismographic stations that in the near future may provide important data. Also, time picks from uniformly reprocessed seismograms may in fact decrease the data noise [*Di Stefano et al.*, 2011] and result in a more accurate inversion. These two improvements of quantity and quality of the data set may in the future result in an even better tomographic model of the crust and uppermost mantle in this area.

Acknowledgments

References

Alessandrini, B., L. Beranzoli, and F. M. Mele (1995), 3-D crustal *P*-wave velocity tomography of the Italian region using local and regional seismicity data, *Ann. Geophys.*, *38*(2), 189–211, doi:10.4401/ag-4119.

Amato, A., B. Alessandrini, G. Cimini, A. Frepoli, and G. Selvaggi (1993), Active and remnant subducted slabs beneath Italy: Evidence from seismic tomography and seismicity, *Ann. Geophys.*, *36*(2), 201–214.

Benoit, M. H., M. Torpey, K. Liszewski, V. Levin, and J. Park (2011), *P* and *S* wave upper mantle seismic velocity structure beneath the northern Apennines: New evidence for the end of subduction, *Geochem. Geophys. Geosyst.*, *12*, Q06004, doi:10.1029/2010GC003428.

Bianchi, I., J. Park, N. Piana Agostinetti, and V. Levin (2010), Mapping seismic anisotropy using harmonic decomposition of receiver functions: An application to Northern Apennines, Italy, *J. Geophys. Res.*, *115*, B12317, doi:10.1029/2009JB007061.

Bleibinhaus, F., and H. Gebrande (2005), Crustal structure of the Eastern Alps along the TRANSALP profile from wide-angle seismic tomography, *Tectonophysics*, *414*, 51–69, doi:10.1016/j.tecto.2005.10.028.

Carminati, E., and C. Doglioni (2012), Alps vs. Apennines: The paradigm of a tectonically asymmetric Earth, *Earth Sci. Rev.*, *112*, 67–96, doi:10.1016/j.earscirev.2012.02.004.

Chiarabba, C., and A. Amato (1996), Crustal velocity structure of the Apennines (Italy) from *P*-wave travel time tomography, *Ann. Geophys.*, *39*(6), 1133–1148, doi:10.4401/ag-4042.

Christensen, N. I., and W. D. Mooney (1995), Seismic velocity structure and compositional of the continental crust: A global view, *J. Geophys. Res.*, *100*(B6), 9761–9788, doi:10.1029/95JB00259.

Cimini, G., and P. De Gori (2001), Nonlinear P-wave tomography of subducted lithosphere beneath central-southern Apennines (Italy), *Geophys. Res. Lett.*, *28*(23), 4387–4390, doi:10.1029/2001GL013546.

Diehl, T., S. Husen, E. Kissling, and N. Deichmann (2009), High-resolution 3-D P-wave model of the Alpine crust, *Geophys. J. Int.*, *179*(2), 1133–1147, doi:10.1111/j.1365-246X.2009.04331.x.

Di Stefano, R., C. Chiarabba, F. Lucente, and A. Amato (1999), Crustal and uppermost mantle structure in Italy from the inversion of *P*-wave arrival times: Geodynamic implications, *Geophys. J. Int.*, *139*, 483–498, doi:10.1046/j.1365-246x.1999.00952.x.

Di Stefano, R., E. Kissling, C. Chiarabba, A. Amato, and D. Giardini (2009), Shallow subduction beneath Italy: Three-dimensional images of the Adriatic-European-Tyrrhenian lithosphere system based on high-quality *P* wave arrival times, *J. Geophys. Res.*, *114*, B05305, doi:10.1029/2008JB005641.

Di Stefano, R., I. Bianchi, M. G. Ciaccio, G. Carrara, and E. Kissling (2011), Three-dimensional Moho topography in Italy: New constraints from receiver functions and controlled source seismology, *Geochem. Geophys. Geosyst.*, *12*, Q09006, doi:10.1029/2011GC003649.

Engdahl, E. R., R. Van Der Hilst, and R. Buland (1998), Global teleseismic earthquake relocation with improved travel times and procedures for depth determination, *Bull. Seimol. Soc. Am.*, *88*(3), 722–743.

Faccenna, C., C. Piromallo, A. Crespo-Blanc, L. Jolivet, and F. Rossetti (2004), Lateral slab deformation and the origin of the western Mediterranean arcs, *Tectonics*, *23*, TC1012, doi:10.1029/2002TC001488.

Gill, P. E., W. Murray, and M. H. Wright, (1982), *Practical Optimization*, 418 pp., Emerald Group Publ. Ltd, Academic Press, London.

Handy, M. R., S. M. Schmid, R. Bousquet, E. Kissling, and D. Bernoulli (2010), Reconciling plate-tectonic reconstructions of Alpine Tethys with the geological-geophysical record of spreading and subduction in the Alps, *Earth Sci. Rev.*, *102*, 121–158, doi:10.1016/j.earscirev.2010.06.002.

Hung, S.-H., F. A. Dahlen, and G. Nolet (2001), Wavefront healing: A banana-doughnut perspective, *Geophys. J. Int.*, *146*, 289–312.

International Seismological Centre (2009), *EHB Bulletin*, Thatcham, U. K. [Available at http://www.isc.ac.uk.].

Kennett, B. L. N., E. R. Engdahl, and R. Buland (1995). Constraints on seismic velocities in the Earth from traveltimes, *Geophys. J. Int.*, *122*, 108–124.

Kissling, E., S. M. Schmid, R. Lippitsch, J. Ansorge, and B. Fgenschuh (2006), Lithosphere structure and tectonic evolution of the Alpine arc: New evidence from high-resolution teleseismic tomography, *Geol. Soc. London Mem.*, *32*, 129–145, doi:10.1144/GSL.MEM.2006.032.01.08.

Kummerow, J., R. Kinda, O. Oncken, P. Giese, T. Ryberg, K. Wylegalla, F. Scherbaum, and TRANSALP Working Group (2004), A natural and controlled source seismic profile through the Eastern Alps: TRANSALP, *Earth Planet. Sci. Lett.*, *225*(12), 115–129.

Lapidus, L., and G. F. Pinder (1982), *Numerical Solution of Partial Differential Equations in Science and Engineering*, John Wiley, New York.

Lévêque, J. J., L. Rivera, and G. Wittlinger (1993), On the use of the checker-board test to assess the resolution of tomographic inversions, *Geophys. J. Int.*, *115*, 313–318, doi:10.1111/j.1365-246X.1993.tb05605.x.

Lippitsch, R., E. Kissling, and J. Ansorge (2003), Upper mantle structure beneath the Alpine orogen from high-resolution teleseismic tomography, *J. Geophys. Res.*, *108*(88), 2376, doi:10.1029/2002JB002016.

Lucente, F., C. Chiarabba, G. Cimini, and D. Giardini (1999), Tomographic constraints on the geodynamic evolution of the Italian region, *Geophys. Res. Lett.*, *104*(B9), 20,307–20,327, doi:10.1029/1999JB900147.

Malinverno, A., and W. Ryan (1986), Extension in the Tyrrhenian Sea and shortening in the Apennines as result of arc migration driven by sinking of the lithosphere, *Tectonics*, *5*(2), 227–245, doi:10.1029/TC005i002p00227.

Marani, M. P., and T. Trua (2002), Thermal constriction and slab tearing at the origin of a superinflated spreading ridge: Marsili volcano (Tyrrhenian Sea), *J. Geophys. Res.*, *107*(B9), 2188, doi:10.1029/2001JB000285.

Mele, G., and E. Sandvol (2003), Deep crustal roots beneath the northern Apennines inferred from teleseismic receiver functions, *Earth Planet. Sci. Lett.*, *211*, 6978, doi:10.1016/S0012-821X(03)00185-7.

Mele, G., A. Rovelli, D. Seber, T. M. Hearn, and M. Barazangi (1998), Compressional velocity structure and anisotropy in the uppermost mantle beneath Italy and surrounding regions, *J. Geophys. Res.*, *103*(B6), 12,529–12,543, doi:10.1029/98JB00596.

Molinari, I., and A. Morelli (2011), EPcrust: A reference crustal model for the European Plate, *Geophys. J. Int.*, *185*(1), 352–364, doi:10.1111/j.1365-246X.2011.04940.x.

Montuori, C., G. Cimini, and P. Favalli (2007), Teleseismic tomography of the southern Tyrrhenian subduction zone: New results from seaflor and land recordings, *J. Geophys. Res.*, *112*, B03311, doi:10.1029/2005JB004114.

Morelli, A., and A. Dziewonski (1993), Body wave traveltimes and a spherically symmetric P- and S-wave velocity model, *Geophys. J. Int.*, *112*, 178–194, doi:10.1111/j.1365-246X.1993.tb01448.x.

Nicolich, R. (2010), Geophysical investigation of the crust of the Upper Adriatic and neighbouring chains, *Rend. Fis. Acc. Lincei*, *21*, suppl. 1, 1530, doi:10.1007/s12210-010-0099-8.

Nolet, G. (1987), Seismic wave propagation and seismic tomography, in *Seismic Tomography*, edited by G. Nolet, pp. 1–23, D. Reidel, Norwell, Mass.

Nolet, G., and F. A. Dahlen (2000), Wave front healing and the evolution of seismic delay times, *J. Geophys. Res.*, *105*(B8), 19,043–19,054.

Paige, C. C., and M. A. Saunders (1982a), LSQR: An algorithm for sparse linear equations and sparse least squares, *ACM Trans. Math. Software*, *8*(1), 43–71.

Paige, C. C., and M. A. Saunders (1982b), LSQR: Sparse linear equations and least squares problems, *ACM Trans. Math. Software*, *8*(2), 195–209.

Papazachos, C. B., and G. Nolet (1997), Non-linear arrival time tomography, *Ann. Geophys.*, *40*(1), 85–97, doi:10.4401/ag-3937.

Piana Agostinetti, N., and A. Amato (2009), Moho depth and V_P/v_S ratio in peninsular Italy from teleseismic receiver functions, *J. Geophys. Res.*, *114*, B06303, doi:10.1029/2008JB005899.

Piana Agostinetti, N., F. Lucente, G. Selvaggi, and M. Di Bona (2002), Crustal structure and Moho geometry beneath the Northern Apennines (Italy), *Geophys. Res. Lett.*, *29*(20), 1999, doi:10.1029/2002GL015109.

Piana Agostinetti, N., V. Levin, and J. Park (2008), Crustal structure above a retreating trench: Receiver function study of the northern Apennines orogen, *Earth Planet. Sci. Lett.*, *275*, 211–220, doi:10.1016/j.epsl.2008.06.02.

Piccinini, D., M. Di Bona, F. P. Lucente, V. Levin, and J. Park (2010), Seismic attenuation and mantle wedge temperature in the northern Apennines subduction zone (Italy) from teleseismic body wave spectra, *J. Geophys. Res.*, *115*, B09309, doi:10.1029/2009JB007180.

Piromallo, C., and A. Morelli (1997), Imaging the Mediterranean upper mantle by P-wave travel time tomography, *Ann. Geophys*, *40*(4), 963–979, doi:10.4401/ag-3890.

Piromallo, C., and A. Morelli (2003), P wave tomography of the mantle under the Alpine-Mediterranean area, *J. Geophys. Res.*, *108*(B2), 2065, doi:10.1029/2002JB001757.

Podvin, P., and I. Lecomte (1991), Finite difference computation of traveltimes in very contrasted velocity models: A massively parallel approach and its associated tools, *Geophys. J. Int.*, *105*, 271–284, doi:10.1111/j.1365-246X.1991.tb03461.x.

Serretti, P., and A. Morelli (2011), Seismic rays and traveltime tomography of strongly heterogeneous mantle structure: Application to the Central Mediterranean, *Geophys. J. Int.*, *187*(3), 1708–1724, doi:10.1111/j.1365-246X.2011.05242.x.

Schmid, S., B. Fügenschuh, E. Kissling, and R. Schuster (2005), Tectonic map and overall architecture of the Alpine orogen, *Eclogae Geol. Helv.*, *97*, 93–117, doi:10.1007/s00015-004-1113-x.

Schmid, S. M., and E. Kissling (2000), The arc of the western Alps in the light of geophysical data on deep crustal structure, *Tectonics*, *19*(1), 62–85, doi:10.1029/1999TC900057.

Solarino, S., E. Kissling, S. Sellami, G. Smriglio, F. Thouvenot, M. Granet, K. P. Bonjer, and D. Slejko (1997), Compilation of a recent seismicity data base of the greater Alpine region from several seismological networks and preliminary 3D tomographic results, *Ann. Geophys.*, *40*(1), 161–174.

Stehly, L., B. Fry, M. Campillo, N. M. Shapiro, J. Giulbert, L. Boschi, and D. Giardini (2009), Tomography of the Alpine region from observations of seismic ambient noise, *Geophys. J. Int.*, *178*(1), 338–350, doi:10.1111/j.1365-246X.2009.04132.x.

Tarantola, A. (2005), *Inverse Problem Theory and Model Parameter Estimation*, Society for Industrial and Applied Mathematics, Philadelphia, Penn.

Tiberti, M., L. Orlando, D. Di Bucci, M. Bernabini, and M. Parotto (2005), Regional gravity anomaly map and crustal

model of the central southern Apennines (Italy), *J. Geodyn.*, *40*, 73–91, doi:10.1016/j.jog.2005.07.014.

Tryggvason, A., and B. Bergman (2006), A traveltime reciprocity discrepancy in the Pdvin & Lecomte *time3d* finite difference algorithm, *Geophys. J. Int.*, *165*, 432–435, doi:10.1111/j1365-246X.2006.02925.x.

Vidale, J. E. (1988), Finite-difference calculation of travel times, *Bull. Seismol. Soc. Am.*, *78*(6), 2062–2076.

Vidale, J. E. (1990), Finite-difference calculation of travel times in three dimensions, *Geophysics*, *55*(5), 521–526.

Wagner, M., E. Kissling, and S. Husen (2012), Combining controlled-source seismology and local earthquake tomography to derive a 3-D crustal model of the western Alpine region, *Geophys. J. Int.*, *191*(2), 789–802, doi:10.1111/j.1365-246X.2012.05655.x.

Waldhauser, F., R. Lippitsch, E. Kissling, and J. Ansorge (2002), High resolution teleseismic tomography of upper-mantle structure using an a priori three-dimensional crustal model, *Geophys. J. Int.*, *150*, 403–414.

Wessel, P., and W. H. F. Smith (1998), New improved version of the Generic Mapping Tools released, *EOS Trans. AGU*, *79*(47), 579, doi:10.1029/98EO00426.

Wielandt, H. (1987), On the validity of the ray approximation for interpreting delay times, in *Seismic Tomography*, edited by G. Nolet, pp. 85–98, Reidel Publishing Co., Dordrecht, Holland.